Preparation of CS-Fe@Fe$_3$O$_4$ nanocomposite as an efficient and recyclable adsorbent for azo dyes removal

Shengyan Pu[a,b,*], Miaoting Wang[a], Kexin Wang[a], Yaqi Hou[a], Jing Yu[a], Qingqing Shi[a], Xiangjun Pei[a,*], Wei Chu[b,*]

[a]*State Key Laboratory of Geohazard Prevention and Geoenvironment Protection, Chengdu University of Technology, 1#, Dongsanlu, Erxianqiao, Chengdu 610059, Sichuan, China, Tel. +86 2884073253; emails: pushengyan@gmail.com, pushengyan13@cdut.edu.cn (S. Pu)*
[b]*Department of Civil and Environmental Engineering, The Hong Kong Polytechnic University, Hong Kong, China*

ABSTRACT

As an effective and in situ purification strategy, adsorption technology has drawn much attention and recently the utilization of biomass substrate has been regarded as a promising way to enhance the adsorption performance and reduce cost. In this study, chitosan was applied as matrix and the magnetic Fe-crosslinked chitosan (CS-Fe@Fe$_3$O$_4$) composite was obtained through a chelation procedure with cheap and environmentally friendly chitosan and iron salts. Then, the resultant CS-Fe@Fe$_3$O$_4$ composites were characterized by scanning electron microscopy, transmission electron microscopy, Fourier-transform infrared spectroscopy, X-ray photoelectron spectroscopy, X-ray diffraction, and thermogravimetric analysis. The sorption and desorption of methyl orange (MO), a common type of azo dye, on CS-Fe@Fe$_3$O$_4$ composite was systematically studied to understand its availability for dyeing wastewater. The results revealed that CS-Fe@Fe$_3$O$_4$ composites could efficiently remove MO in a wide pH range. The mixed Fe$_3$O$_4$ particles were physically mixed and almost had no negative effect on its adsorption. Moreover, the dye adsorption process was found to be controlled by the pseudo-second-order rate model and the adsorption isotherm behavior could be described by the Langmuir model. The repeatability test showed that the CS-Fe@Fe$_3$O$_4$ composites could retain its high efficiency after desorption and regeneration. In summary, the results presented herein indicated that the resultant CS-Fe@Fe$_3$O$_4$ nanocomposite with high adsorption efficiency and strong magnetic property could serve as a potential adsorbent for remediating industrial dyeing wastewater.

Keywords: Fe-crosslinked chitosan; Magnetic adsorbent; Azo dyes; Adsorption kinetics

1. Introduction

Dyes, as natural and synthetic organic compounds, have been extensively applied in many industries, such as the production of textile, paper and pulp, clothing, tannery, paint, printing, and the effluents of these industries tend to contain dyes in excessive quantities. Therefore, the discharge of dyeing wastewater has caused severe environmental problems due to its high chromaticity, poor biodegradability and the containing bio-recalcitrant components [1]. Importantly, most dyes or dye intermediates are highly carcinogenic and teratogenic, which may lead to harm to human health as well as the ecological environment [2]. Among typical dyes, azo dyes with nitrogen–nitrogen double bonds and complex aromatic structures are of the largest production and have the greatest versatility [3]. Hence, to develop efficient techniques to remediate and purify dyeing wastewater is imminent and urgent [4–6]. Until now, some conventional methods, such as flocculation [7,8], microbiological treatment [9], membrane filtration [10], or electrochemical treatment [11], advanced oxidation [12], have been employed in dyeing wastewater treatment [13].

* Corresponding author.

However, the high cost and large sludge production greatly limit the application of the conventional technologies above [14]. Adsorption [5], as an effective purification strategy, has been considered to be one of the most potential alternatives for dyeing wastewater treatment due to its simplicity and wide adaptability [15,16]. Therefore, current research mainly focuses on preparing and synthesizing cost-effective and practical adsorbents in dyeing wastewater treatment [17]. Up to now, various adsorbents have already been prepared, such as natural biopolymers [18], agricultural residues [14] and industrial solid wastes [19]. Among them, chitosan, a type of natural polysaccharide and deacetylated product of the natural biopolymer chitin, is regarded as a promising alternative [20] due to its strong adsorption functions [21]. Whereas the direct utilization of chitosan as the adsorbent is still unsatisfactory because of its weak acid-resistance, non-selective adsorption and poor mechanical properties [4,22]. To overcome these issues, further modification is necessary.

The synthesis of metal-binding biopolymer not only promotes the studies of the interaction of polymers with metal ions [22] but also provides some further information about biopolymers' property, such as its high sorption capacity, excellent chemical stability and strong mechanical property [17,23]. During the preparation of metal–chitosan composite, (a) metal ions can coordinate with –OH and –NH_2 in chitosan and produce stable coordination complexes; (b) metal ion coordination cross-links chitosan chains and strengthens their stability; (c) the high viscosity of chitosan can limit the growth of particle size of metal hydrolysate, which leads to a more homogenous dispersion [21,24]. As a result, the as-formed metal-modified chitosan derivative draws much attention as an adsorbent in wastewater treatment [3]. Among them, the Fe-crosslinked chitosan complex is undoubtedly the most popular one because of its relatively low-cost and good applicability, easy operation, stable molecular structure and good reusability [23,25]. Furthermore, its utilization has been extended in many fields, such as dyes [26], Cr(VI) [27], As(V) [24], fluoride [28], and organophosphorus pesticides [29] wastewater treatment. However, after adsorption, the separation problem is still to be solved, especially the typical powder adsorbent, and the residuary may cause unnecessary waste and generate secondary pollution. To solve this problem, magnetic separation technology has been applied [30].

In this study, an economical and practical magnetic sorbent, CS-Fe@Fe_3O_4, was prepared through chelation of cheap and environmentally friendly chitosan with iron ion and its adsorption property was systematically characterized using methyl orange (MO) as the model contaminant (Section 1, Supporting Information). The adsorption and reusability were systematically studied in batch experiments. Furthermore, through data analysis, possible mechanism of the material formation and adsorption were proposed. In summary, this study may provide a facile, promising and environmentally friendly strategy for the preparation of efficient absorption material and its application in dyeing wastewater treatment.

2. Materials and methods

2.1. Chemicals

Chitosan (CS, deacetylation degree ≥95%, viscosity = 100–200 mPa·s) was obtained from Aladdin Reagent Co., Ltd.

(Shanghai, China). Fe_3O_4 particles (OD = 200 nm, purity >99.5%) were purchased from Macklin Reagent Co., Ltd. (Shanghai, China). Hexahydrate ferric chloride ($FeCl_3 \cdot 6H_2O$), glutaraldehyde ($C_5H_8O_2$, 25%), and anhydrous ethanol (C_2H_5OH), all of analytical grade were obtained from Kelong Chemical Reagent Factory (Chengdu, China). MO was purchased from Ruijin special Chemical Co., Ltd. (Tianjin, China). Deionized (DI) water used for all experiments was generated from Milli-Q water purification system (Ulupure Corporation, Chengdu, China).

2.2. Preparation of CS-Fe@Fe_3O_4

The complex was synthetized by a modified method according to the procedure described in literature [31]. Specifically, 1.0 g CS was dissolved in 50 mL 0.1 M $FeCl_3$ aqueous solution, and the mixture was magnetically stirred for 4 h to adequately chelate the Fe^{3+} with the CS. Then, 0.1 g Fe_3O_4 particles were added to the solution and dispersed sufficiently by mechanical agitation in order to make them magnetized. Next, precipitation was obtained by adding ethanol into the above mixture. The precipitated solid was washed with ethanol several times to remove the excess iron ions and dried at 80°C under vacuum conditions. Furthermore, the obtained solid was intensively grinded, and slowly placed into a 5% glutaraldehyde ethanol solution for 2 h at 30°C, letting CS and glutaraldehyde chemically crosslink to enhance the stability of the composites. Thereafter, the composites were collected through an external magnetic field and washed with DI water to remove residual glutaraldehyde and ethanol. After vacuum drying at 80°C, the CS-Fe@Fe_3O_4 was obtained. In order to verify the effect of the mixed Fe_3O_4, the non-magnetic Fe-crosslinked chitosan (CS-Fe) was prepared under the same condition (Section 2, Supporting Information).

2.3. Characterization

The micromorphology of samples was characterized with a scanning electron microscope (JSM-7500F, Japan) and a transmission electron microscope (Tecnai-G20, USA). XRD patterns of CS, CS-Fe and CS-Fe@Fe_3O_4 were recorded on an X-ray diffractometer (Rigaku Ultima IV, Japan) with a Cu-Kα radiation. FTIR spectra were obtained on a Fourier-transform infrared spectroscope (Nicolet-460, USA). X-ray photoelectron spectra (XPS) were performed on a Thermo Fisher Scientific standard (K-Alpha, USA). Thermogravimetric analysis was carried out in a simultaneous thermal analyzer (Netzsch STA 449F3, Germany) at a heating rate of 10 K/min from 20°C to 800°C under an argon gas atmosphere. The magnetism of the sample was investigated between ±20 K O_e at 298 K using a vibrating sample magnetometer (Squid-VSM, USA).

2.4. Adsorption experiments

Typically, 200 mg/L MO simulated wastewater mixed with a certain amount of CS-Fe@Fe_3O_4 was agitated in a thermostatic water bath oscillator (JBXL-70, China) at 150 rpm in batch adsorption experiments. The influence of the adsorbent dosage (0.2–1.6 g/L), the initial pH value (3, 5, 7, 9 and 11),

the contact time and the reaction temperature (5°C, 15°C, 25°C and 35°C) were investigated. The initial pH value was adjusted by 0.1 M NaOH and 0.1 M HCl. After the adsorbent was separated via external magnetic field, the residual concentration of MO was measured by a visible spectrometer (V-1100D, China) at a wavelength of 465 nm. For the kinetic study, a fixed amount of CS-Fe and CS-Fe@Fe$_3$O$_4$ was added into 50 mL of MO aqueous solution at 25°C. At selected time intervals, a certain volume of supernatant was collected and the residual concentration of MO was measured. For the adsorption isotherm study, the same amount of CS-Fe@Fe$_3$O$_4$ was mixed with MO solution of different concentrations from 50 to 2,000 mg/L. After equilibrium was reached, the concentration of the supernatant was analyzed as described above.

The removal rate (η) of MO in % and the amount of adsorbent (q_t) in mg/g at time t were calculated by Eqs. (1) and (2).

$$\eta = \frac{c_t}{c_0} \times 100\% \tag{1}$$

$$q_t = \frac{(c_0 - c_t)V}{W} \tag{2}$$

where c_0 (mg/L) is the initial concentration of MO aqueous solution, c_t (mg/L) is the concentration of MO at time t, V (L) is the volume of MO aqueous solution, and W (g) is the dose of adsorbent.

3. Results and discussion

3.1. Preparation of CS-Fe@Fe$_3$O$_4$

The preparation of CS-Fe@Fe$_3$O$_4$ was based on the Lewis electronic theory of acid and alkali, where the alkali donated a pair of electrons to the acid. CS has two types of binding sites, the hydroxyl group (–OH) and the amino group (–NH$_2$), which were typical hard Lewis alkali groups likely to bind with a hard Lewis acid (such as Fe^{3+}) to form a stable complex structure [32]. Besides, the Fe^{3+} played a bridge-like role in cross-linking two or more CS chains by connecting –OH or –NH$_2$. The proposed preparation mechanism of CS-Fe@Fe$_3$O$_4$ is shown in Fig. 1.

As a result, a supramolecular polymeric network was formed to enhance the stability of CS. In addition, CS as template could evenly disperse in the hydrolysis of Fe^{3+} and control the growth of particles, leading to uniformly sized amorphous iron oxides [23,33]. The Fe in the structure of chelating CS with Fe was hexacoordinated, with two molecules of CS monomer through complexation with –NH$_2$ and –OH in coordination sphere of Fe [34]. Other coordination sites were filled with water molecules or other ions in aqueous solution, thus completing the coordination sphere and forming a stable clathrate. The Fe$_3$O$_4$ particles were mixed with the clathrate to introduce magnetic property, which allowed to magnetically separate the complex from aqueous phase.

3.2. Characterization

3.2.1. Scanning electron microscope

SEM images of CS-Fe and CS-Fe@Fe$_3$O$_4$ are shown in Figs. 2(A)–(C). They illustrate that the samples were non-porous and had a smooth, irregularly laminated structure. However, it could be observed that there were some particles with a diameter of about 200 nm dispersed on the surface of CS-Fe@Fe$_3$O$_4$ (Figs. 2(B) and (C)) which was in accordance with the size of added Fe$_3$O$_4$ particles.

3.2.2. Transmission electron microscope

The TEM images of CS-Fe and CS-Fe@Fe$_3$O$_4$ were shown in Figs. 2(D)–(G). The large amounts of circular particles with a diameter of less than 10 nm were distributed uniformly inside the samples (Figs. 2(D) and (E)) and probably the amorphous iron oxides produced through hydrolysis [33]. Fig. 2(G) shows that some particles with a diameter 200 nm were successfully incorporated into the CS-Fe@Fe$_3$O$_4$ composites; however, these particles are not observed in Fig. 2(F).

3.2.3. X-ray diffraction

The XRD patterns of CS, CS-Fe and CS-Fe@Fe$_3$O$_4$ are presented in Fig. 3. According to early literature [8], the wide peak in the range of $2\theta = 9°–23°$ was assigned to the amorphous region of CS. When the CS interacted with Fe^{3+}, there was a large change in the XRD spectra at $2\theta = 9 –23°$ due to the cross-linking reaction. Meanwhile, two new broad peaks appeared at about 24° and 35° which were

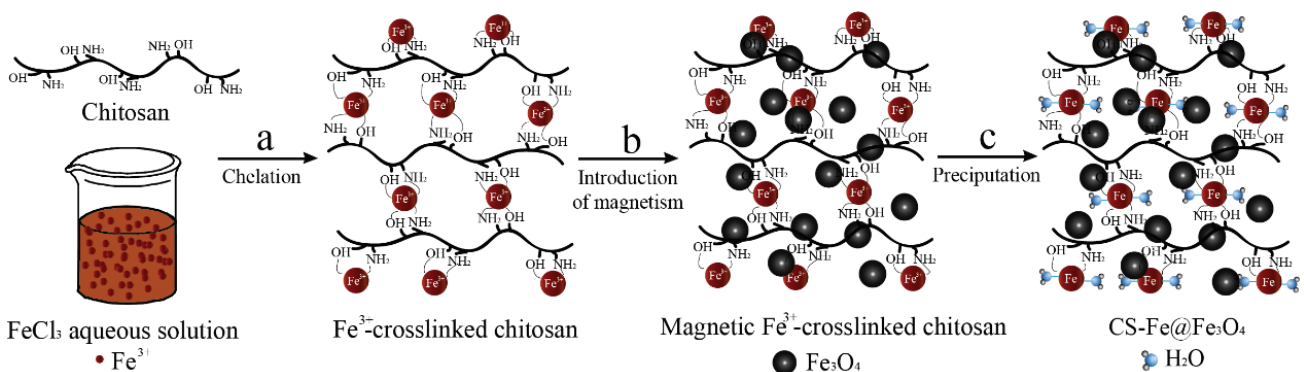Fig. 1. Preparation of CS-Fe@Fe$_3$O$_4$: (a) chelating Fe^{3+} with CS, (b) mixing Fe$_3$O$_4$ particles to introduce magnetism, and (c) formation of CS-Fe@Fe$_3$O$_4$.
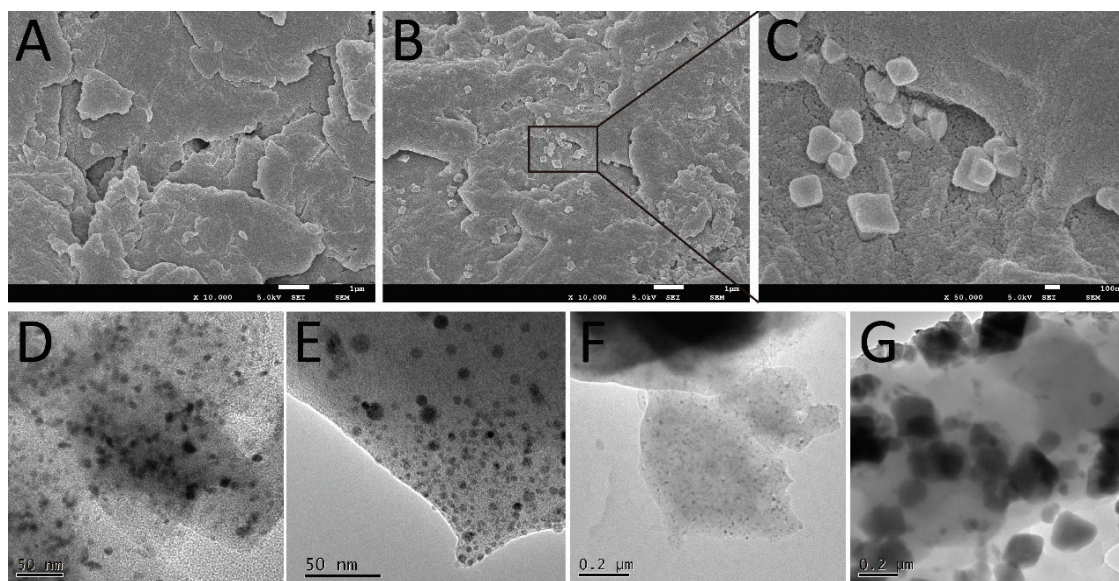
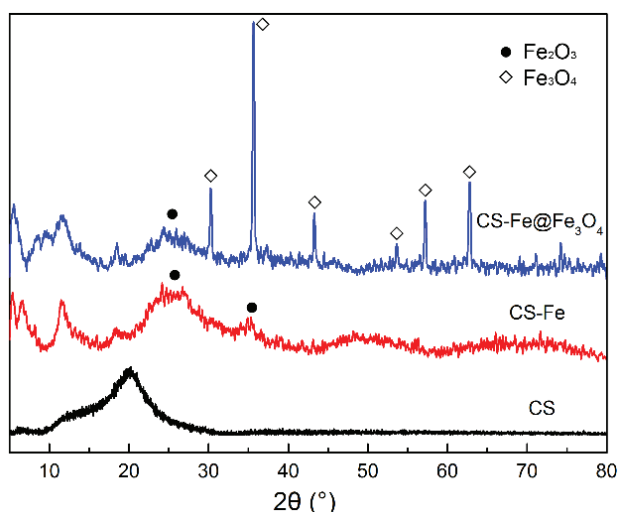Fig. 2. SEM images of (A) CS-Fe, (B,C) CS-Fe@Fe_3O_4; TEM images of (D,F) CS-Fe and (E,G) CS-Fe@Fe_3O_4.

Fig. 3. XRD patterns of CS, CS-Fe and CS-Fe@Fe_3O_4.

associated to Fe_2O_3 (JCPDS 33-0664). A light change was also observed in $2\theta = 40$ –$80°$. These changes evidenced that the strong chelation happened between CS and Fe centers. Compared the XRD spectra of CS-Fe with CS-Fe@Fe_3O_4, the curves were similar, but some new sharp peaks appeared in CS-Fe@Fe_3O_4 which were in good agreement with the standard values for Fe_3O_4 (JCPDS 19-0629). It illustrated that Fe_3O_4 particles existed in CS-Fe@Fe_3O_4 and had no effect on its structure.

3.2.4. Fourier-transform infrared spectroscope

The FTIR spectra of CS, CS-Fe and CS-Fe@Fe_3O_4 are shown in Fig. 4. In the spectrum from 3,000 to 4,000 cm⁻¹ (Fig. 4(A)), the spectrum of CS presented a υ_{OH} band at 3,430 cm⁻¹ and υ_{NH} at 3,369 cm⁻¹ [35], while the spectrum of CS-Fe only showed one peak at 3,423 cm⁻¹. These signals

shifted almost 7 cm⁻¹ below and 54 cm⁻¹ above the original υ_{OH} and υ_{NH} values, respectively, which indicated the change of functional groups of CS [32]. The bands of δ_{NH2} before and after complexing were presented at 1,598 and 1,522 cm⁻¹, respectively, almost 76 cm⁻¹ lower, due to the existence of ligand [36], which was in agreement with the spectral behavior of N–H in the 3,000–4,000 cm⁻¹ region, thus indicating the –NH_2 of CS participated in the combination with Fe. Furthermore, Fig. 4(A) shows that the δ_{OH} band at 1,380 cm⁻¹ and the υ_{CO} bands from C3-OH at 1,158, 1,076 and 1,030 cm⁻¹ maintained their original position, while the intensity of the signal was lower than before. Together with the change of the O–H spectra in the 3,000–4,000 cm⁻¹ region, it revealed the combination of –OH in position C3 on CS [32].

There were several new peaks appearing in 400–600 cm⁻¹ region in the spectra of CS-Fe (Fig. 4(B)), which represented the metal–ligand adsorption bands. The peaks at 560 and 481 cm⁻¹ were due to Fe–N, and the bands at 449 and 431 cm⁻¹ expressed the presence of Fe–O. As a result, the –OH and –NH_2 of CS were involved in the strong complexation reaction with Fe, forming a stable metal–biopolymer complex system. Simultaneously, Fig. 4(A) shows that the spectrum of CS-Fe@Fe_3O_4 composite was extremely similar to that of CS-Fe, which may reveal that the Fe_3O_4 particles were rather physically mixed than of chemically bonded.

3.2.5. X-ray photo-electron spectroscopy

The FTIR analysis showed that the mixed Fe_3O_4 was not chemically bonded. Hence, in order to further study the structure of CS-Fe@Fe_3O_4, an XPS analysis of CS-Fe was carried out, as presented in Fig. 5.

In the standard spectrum of $FeCl_3$, the binding energy of Fe2p photo-electrons was at 711.2 eV [25]. However, in the spectrum of Fe2p (Fig. 5(B)), the fitted peaks of Fe2p were at 710.6 and 724.4 eV with shake-up satellite-peaks at 713.1 and
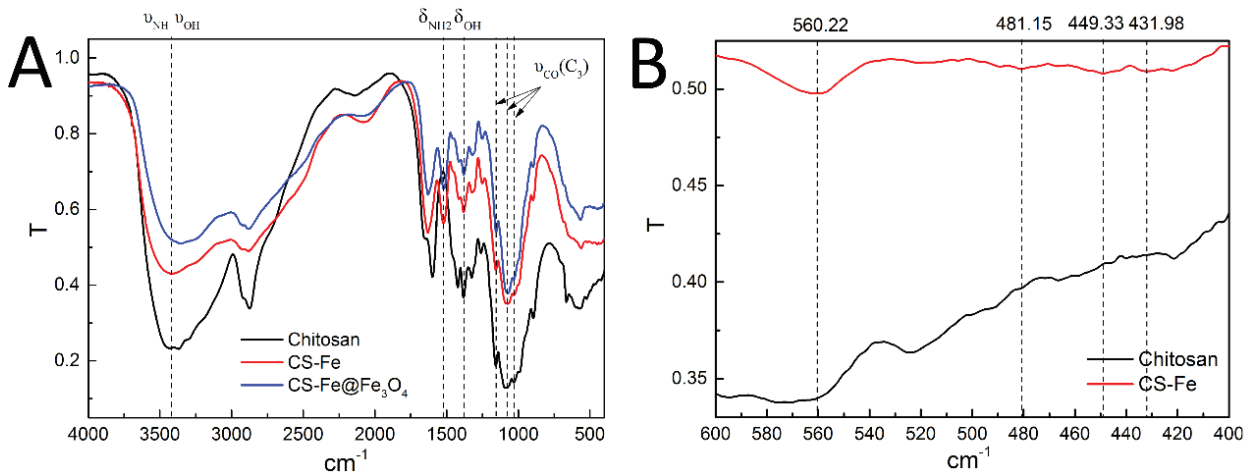
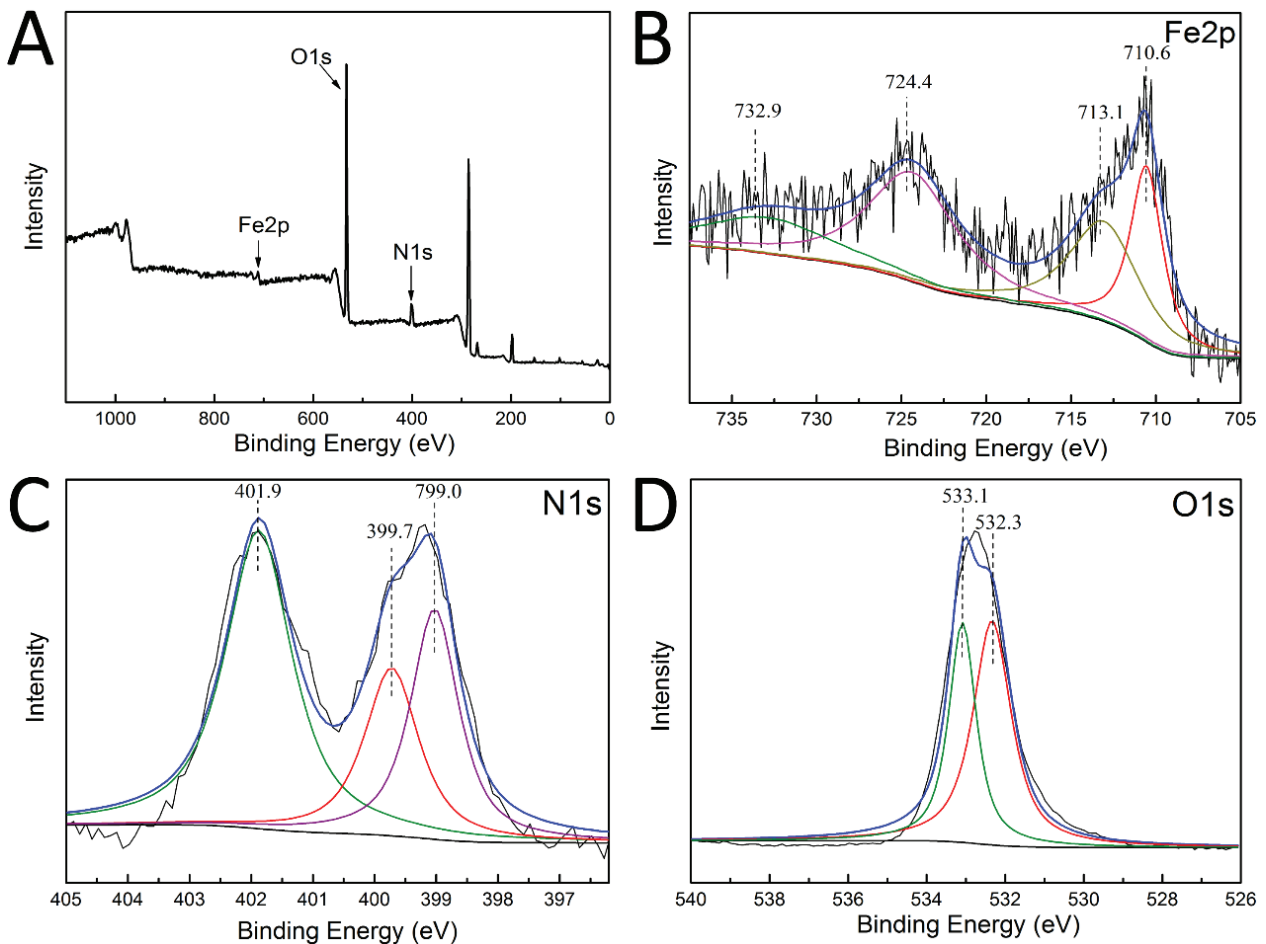Fig. 4. FTIR spectra of CS, CS-Fe and CS-Fe@Fe$_3$O$_4$.

Fig. 5. XPS spectra of CS-Fe: (A) survey, (B) Fe2p, (C) N1s and (D) O1s.

732.9 eV, suggesting the presence of two kinds of bonds with Fe in the structure of CS-Fe.

Fig. 5(C) shows the N1s fitted peaks at binding energy of 399.0, 399.7 and 401.9 eV indicating the nitrogen in –NH$_2$ interacted with the Fe(III), –NH$_2$ and –NH$_3^+$ groups in CS.

The spectrum of O1s fitted with two peaks at binding energies of 532.3 and 533.1 eV (Fig. 5(D)). The first one represented –OH oxygen chelated with Fe, and the second one was –OH oxygen without chelation. The results were in agreement with the FTIR analytic results.

3.2.6. Thermogravimetric analysis

The thermal behavior of CS-Fe, CS-Fe@Fe$_3$O$_4$ and the MO-loaded CS-Fe@Fe$_3$O$_4$ are shown in Fig. 6. Four weight loss stages could be distinguished for CS-Fe, and the weight loss of CS-Fe@Fe$_3$O$_4$ could be divided into five stages where the first four stages were similar to CS-Fe. The first stage related to the evaporation of water including free and bound water between 25 C and 80°C. The second loss, in the interval of 220°C–280°C, related to chain scissions, producing gradually a lot of biopolymer monomers. These processes were followed by the third and fourth stages, related to the breaking up of glucose rings and carbonization, respectively. However, the TG curve of CS-Fe@Fe$_3$O$_4$ shows an additional fifth stage of weight loss, which might indicate the decomposition of Fe$_3$O$_4$ due to the reduction of carbon produced by the carbonization of organic matter and is in accordance with an extra-peak at about 675°C in Fig. 6(B). Overall, the results revealed that the mixed Fe$_3$O$_4$ had no noticeable influence on the thermal behavior of the complex.

After MO adsorption by CS-Fe@Fe$_3$O$_4$, the thermal stability of MO-loaded CS-Fe@Fe$_3$O$_4$ could be enhanced and the decomposition rate decreased, which indicated the formation of a more stable complex (Fig. 6(A)). Similarly, Fig. 6(B) shows that the peak at 245°C for CS-Fe@Fe$_3$O$_4$ meant that the chains were breaking up, whereas the peak appeared at higher temperature (270°C) for MO-loaded CS-Fe@Fe$_3$O$_4$, and the intensity of the peak strongly decreased. Hence, the adsorption of MO by CS-Fe@Fe$_3$O$_4$ promoted the formation of a more thermally stable complex [17].

3.2.7. Vibrating sample magnetometer

Fig. 7 illustrates the magnetization curve of CS-Fe@Fe$_3$O$_4$. The saturation magnetization (M_S) was found to be 4.24 emu/g, which was higher than in previous reports [37,38]. Considering the M_S value of bulk magnetite (92 emu/g) and the Fe-crosslinked chitosan content (more than 90%), the value of saturation magnetization expected to be less than 9.2 emu/g. The reduction of M_S value could be attributed to the presence of surrounded biopolymers [39] and the surface disorder due to the interaction between CS and Fe$_3$O$_4$ particles surface [38]. As can be seen in Fig. 7, the magnetic

saturations of CS-Fe@Fe$_3$O$_4$ were sufficient to separate them from solution by a magnet.

3.3. Adsorption behavior

3.3.1. Effect of adsorbent dosage

A good adsorbent should have a high adsorption capacity, which meant that it should adsorb a large amount of adsorbates at a low adsorbent dosage. Fig. 8(A) shows the effect of adsorbent dosage towards MO with a contact time of 30 min at 25°C at the natural pH value. It illustrates that the removal rate initially increased with dosage increasing. The more adsorbent was added, the more adsorption sites and larger surface area could be formed. Therefore, the removal efficiency increased. More than 99% of MO could be removed by 0.6 g/L of CS-Fe@Fe$_3$O$_4$. Above 0.6 g/L, the removal rate remained almost unchanged. Hence, in order to ensure a good adsorption effect, the 0.6 g/L dosage was used for the following experiments.

3.3.2. Effect of contact time

Fig. 8(B) shows the removal rate of MO as a function of the contact time with CS, CS-Fe and CS-Fe@Fe$_3$O$_4$, respectively,
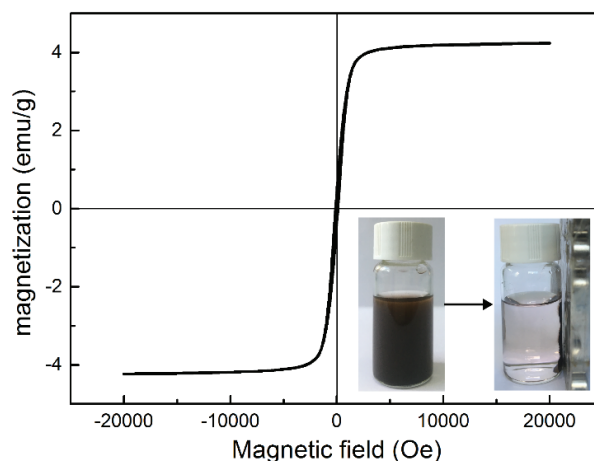

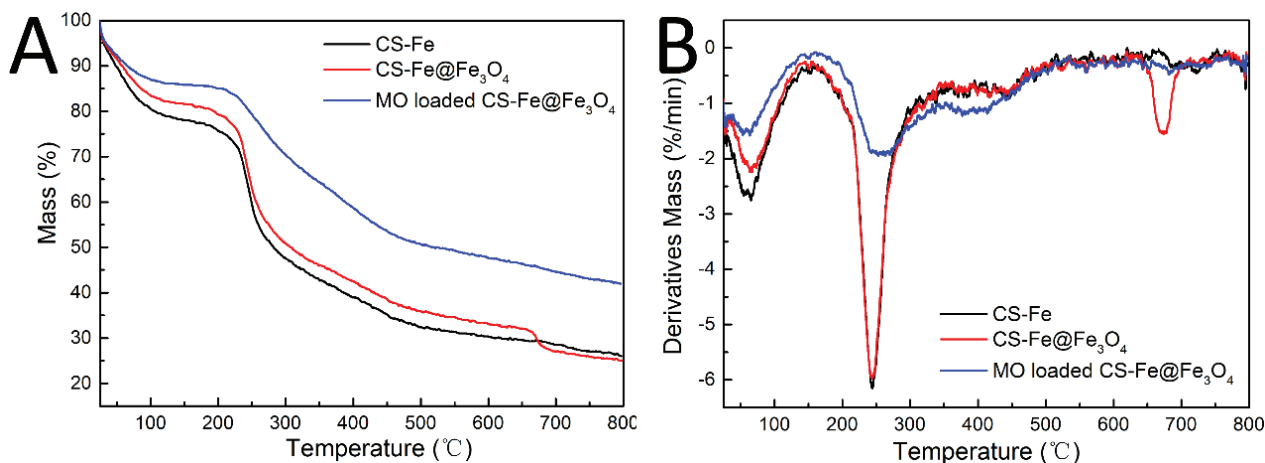Fig. 7. Magnetization curve of CS-Fe@Fe$_3$O$_4$.

Fig. 6. The thermal behavior of CS-Fe, CS-Fe@Fe$_3$O$_4$ and MO loaded CS-Fe@Fe$_3$O$_4$: (A) TG curves and (B) DTG curves.
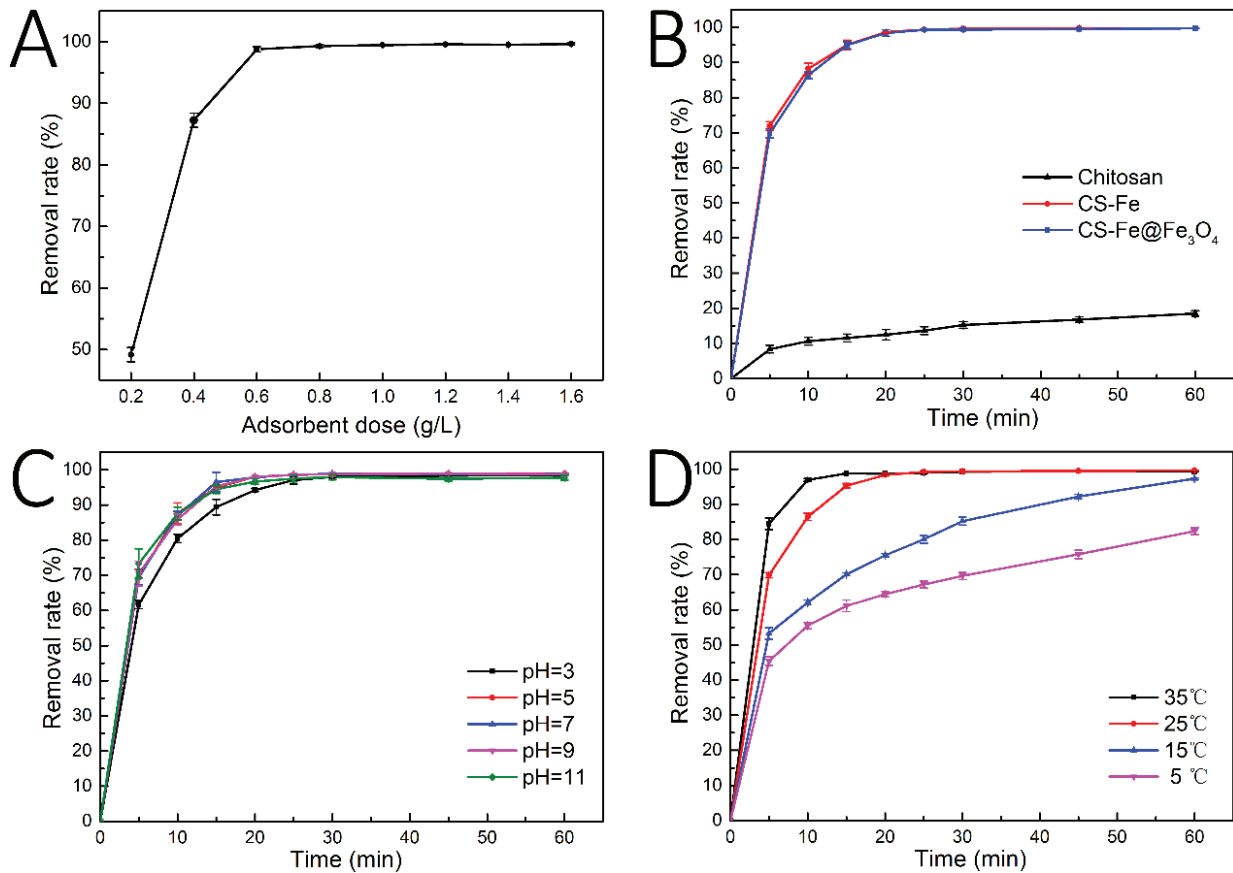
Fig. 8. Batch experiments: (A) the effect of adsorbent dosage, (B) the effect of contact time, (C) the effect of initial pH and (D) the effect of temperature on removal rate of MO.

with 0.6 g/L dosage and natural pH at 25°C. Compared with CS, CS-Fe and CS-Fe@Fe$_3$O$_4$ showed a higher adsorption efficiency under the same condition. Importantly, the complex based on chelating CS with Fe^{3+} greatly enhanced the adsorption capacity in comparison with CS. The added Fe$_3$O$_4$ particles had no effect on its adsorption property. From the adsorption curve of CS-Fe@Fe$_3$O$_4$, the initial removal rate of MO increased rapidly with increasing contact time. After 25 min, the removal rate was above 99%. Later, efficiency remained almost constant, which meant that the adsorption has reached an equilibrium. On the initial stage of adsorption, a large amount of dye could be adsorbed on the surface of the adsorbent. As the adsorption went on, the concentration of MO gradually reduced, decreasing the driving force and slowing down the adsorption rate until reaching the equilibrium. In the adsorption process, the dye molecules on the surface of the adsorbent were rearranged to get more adsorption sites [40].

3.3.3. Effect of initial pH value

The pH value of the solution played an important role in dye adsorption because the initial pH had a strong effect on the surface charge of the adsorbent, the dissociation of functional groups on the binding sites, and the morphology and chemistry of the adsorbate [41]. The effect of initial pH on MO removal was studied in a series of tests with an initial pH values at 3, 5, 7, 9, 11, a contact time of 1 h, and 0.6 g/L dosage at 25°C. Fig. 8(C) showed the effect of initial pH on the MO removal rate. It was obvious that when the initial pH increased from 3 to 11, the removal rate of MO by CS-Fe@Fe$_3$O$_4$ decreased slightly, but the adsorption efficiency above 97% still could be reached at pH = 11. In the adsorption process, two mechanisms, electrostatic interaction and chelation were assumed. In acidic conditions, the free –NH$_2$ of CS and the –SO$_3$Na of MO were forming –NH$_3^+$ and –SO$_3$H, resulting in the formation of –NH$_3^+$–SO$_3^-$ ion pair via electrostatic interaction [23], while the chelation between the dye molecules and the Fe center occurred in a wide range of pH values. These experimental results illustrated that the strong coordination between dye molecules and Fe centers played a main role in the process of adsorption and provided a larger adsorption capacity for CS-Fe@Fe$_3$O$_4$. Meanwhile, the application of CS-Fe@Fe$_3$O$_4$ could better adapt the change of pH, so the initial pH did not need to be adjusted in the subsequent adsorption experiments.

3.3.4. Effect of temperature

Fig. 8(D) shows the effect of temperature on the removal rate of MO adsorbed on CS-Fe@Fe$_3$O$_4$. The pH value of dye solution kept natural and the dosage of adsorbent was 0.6 g/L. It illustrated that the removal rate increased with increasing temperature, and the adsorption percentage enhanced from

82.4% to 99.4% as the temperature increased from 5 C to 35°C. This might be due to the faster diffusion rate of the dye molecule and the lower solution viscosity at higher temperatures. Hence, a higher temperature was favorable for the adsorption of MO onto CS-Fe@Fe_3O_4.

3.3.5. Adsorption kinetics

Adsorption kinetics models were used to describe the rate of the interaction between the adsorbent and the adsorbate and to propose potential rate-controlling and adsorption mechanism. The kinetics of adsorbing MO on CS-Fe@Fe_3O_4 were studied by varying the initial dye concentration at 50, 100, 200 and 300 mg/L, with a contact time of 1 h at 25°C. The pH value of dye solution kept natural and the dosage of adsorbent was 0.6 g/L (Fig. 9(A)). In this study, kinetic data were obtained by fitting the linear forms of the pseudo-first-order (Fig. 9(B)) and pseudo-second-order rate models (Fig. S1, Supporting Information).

Fig. 9(A) shows that the adsorption process of MO onto CS-Fe@Fe_3O_4 was initially fast and eventually reached the equilibrium. The adsorption amount of MO increased with increasing initial dye concentration because higher MO concentration provided a stronger driving force for the mass transfer, thus resulting in more frequent collisions between molecules and the active sites on CS-Fe@Fe_3O_4. The calculated kinetic parameters for the adsorption of MO onto CS-Fe@Fe_3O_4 are presented in Table 1.

By comparing the correlation coefficient value (R^2), it could be obviously concluded that the pseudo-second-order

rate model fitted better (Fig. 9(B)) and the q_e values obtained were in good agreement with the experimental data. It indicated that the overall adsorption process was controlled by chemisorption [4].

3.3.6. Adsorption isotherms

The adsorption reaction properties between adsorbent and adsorbate as well as the definition of the equilibrium state were predicted by adsorption isotherms. In this study, the adsorption isotherm experiments were performed by setting a series of initial MO concentrations in the range of 50 to 2,000 mg/L at the temperatures of 288, 298 and 308 K, respectively, with 0.6 g/L dosage and natural pH (Fig. 10(A)).

Langmuir (Fig. 10(B)), Freundlich (Fig. S2, Supporting Information), Temkin (Fig. S3, Supporting Information), Dubinin–Kaganer–Radushkevich (Fig. S4, Supporting Information) and Flory–Huggins (Fig. S5, Supporting Information) isotherm model were applied to describe the adsorption isotherm for MO onto CS-Fe@Fe_3O_4. The equations of these five isotherm models were listed in Section 4 of Supporting Information. The experimental data were fitted by the five isotherm models and the isotherm parameters are listed in Table 2.

Comparing the R^2 value obtained by the different isotherm models, the Langmuir model provided the highest value, suggesting the homogeneity of CS-Fe@Fe_3O_4 surface and monolayer coverage of MO onto the adsorbent. The maximum adsorption capacities were also obtained using the Langmuir model, that is, 1,087.0, 1,149.4 and 1,219.5 mg/g at
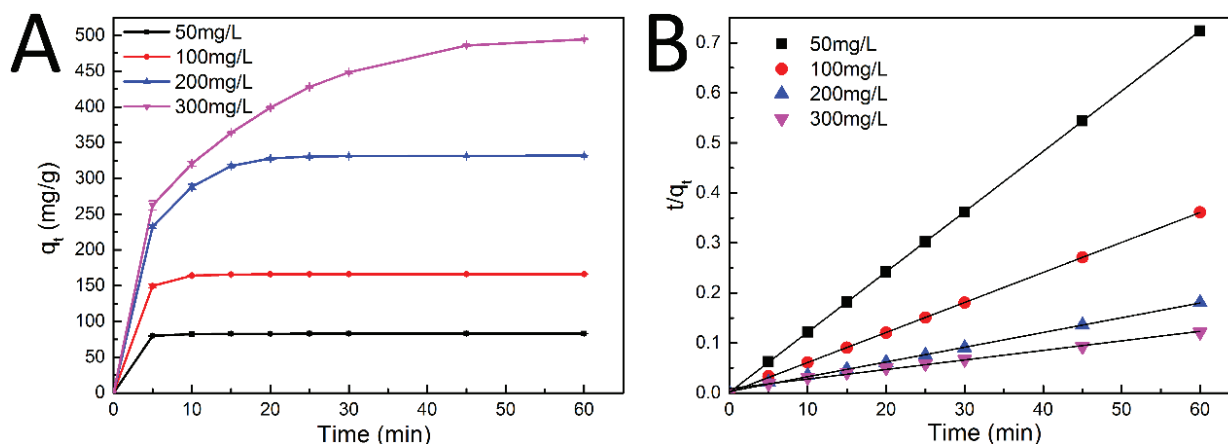

Fig. 9. The kinetics of MO adsorption onto CS-Fe@Fe_3O_4 for different initial concentrations: (A) adsorption kinetics and (B) plot for the pseudo-second-order model.

Table 1
Calculated kinetic parameters for the adsorption of MO onto CS-Fe@Fe_3O_4

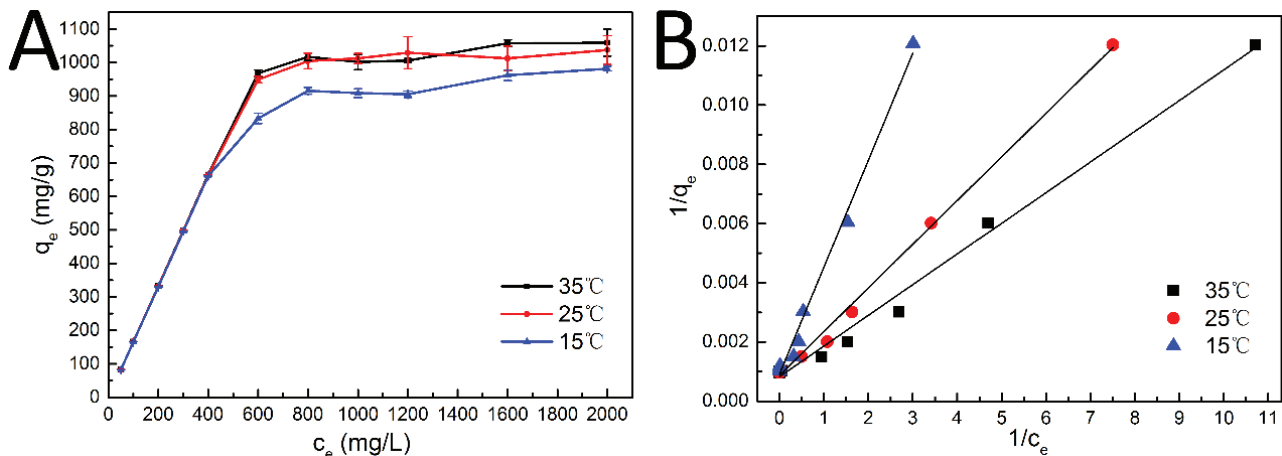| Initial concentration (mg/L)	Experimental (mg/g)	Pseudo-first-order equation			Pseudo-second-order equation		
		q_e (mg/g)	k_1 (1/min)	R^2	q_e (mg/g)	k_2 (1/min)	R^2
50	83.11	4.41	0.0693	0.5005	83.33	0.1440	1.0000
100	166.25	9.63	0.0925	0.5666	166.67	0.0360	0.9999
200	332.11	131.21	0.1369	0.9254	344.83	0.0027	0.9988
300	498.78	429.75	0.0763	0.9927	555.56	0.0003	0.9983

Fig. 10. The isotherm of MO onto CS-Fe@Fe$_3$O$_4$: (a) adsorption isotherm and (b) plot for Langmuir isotherm model.

Table 2
Isotherm parameters for the adsorption of MO onto CS-Fe@Fe$_3$O$_4$

Isotherms	Parameter	Temperature		
		288 K	298 K	308 K
Langmuir	q_{max} (mg/g)	1,087.0	1,149.4	1,219.5
	k_L	0.2548	0.5878	0.7885
	R^2	0.9915	0.9968	0.9926
Freundlich	k_F	245.35	303.28	332.45
	$1/n$	0.2215	0.2083	0.1953
	R^2	0.7419	0.7432	0.7197
Temkin	k_T	24.631	65.407	127.10
	B	98.850	99.799	95.031
	B	24.223	24.826	26.946
	$R2$	0.9057	0.9052	0.8879
Dubinin–Kaganer–Radushkevich	B	2.3×10^{-7}	9×10^{-8}	7×10^{-8}
	Q_m (mg/g)	765.82	865.68	912.06
	E (kJ/mol)	1,474.4	2,357.0	2,672.6
	R^2	0.8701	0.9149	0.9447
Flory–Huggins	k_a	4,222.8	4,144.8	3,973.8
	n	0.6777	0.5746	0.5240
	R^2	0.8480	0.8629	0.8487

the temperatures of 288, 298 and 308 K, respectively, which could be confirmed with the practical experimental data. Besides, the Temkin and Dubinin–Kaganer–Radushkevich models had a better applicability than Freundlich and Flory–Huggins models. For Dubinin–Kaganer–Radushkevich model, the maximum adsorption capacities, 765.82 mg/g at 288 K, 865.68 mg/g at 298 K and 912.06 mg/g at 308 K, were lower than the Langmuir adsorption capacities, which might be due to the different assumptions of these models [42] and different values R^2. The values of E, calculated by Eq. (8) in supporting information at different temperature, were found to be greater than 16 kJ/mol, indicating that the adsorption process for MO onto CS-Fe@Fe$_3$O$_4$ was chemisorption, which agreed with the result of adsorption kinetics (Section 3.3.5). In addition, it could be concluded that the energy binding of sites of adsorbent was uniform, known from the Temkin model.

3.3.7. Adsorption thermodynamics

Our study showed that the adsorption process of MO on CS-Fe@Fe$_3$O$_4$ was affected by the temperature. Therefore, the thermodynamic parameters, including enthalpy (ΔH), entropy (ΔS) and free energy (ΔG) were helpful to understand the adsorption process and properties. The values of thermodynamic parameters over the temperature range 288 to 308 K were calculated and are listed in Table 3 (Section 5, Supporting Information).

Negative values of ΔG suggested the adsorption process was generally spontaneous and the degree of spontaneity increased with the increasing temperature. A positive value of ΔS indicated that the degree of freedom increased at the solid–liquid interface, resulting in more disorder in the system during the adsorption of MO to CS-Fe@Fe$_3$O$_4$.

Table 3
Adsorption thermodynamic parameters of CS-Fe@Fe$_3$O$_4$

Temperature (K)	ΔG (kJ/mol)	ΔH (KJ/mol)	ΔS (J/(mol·K))
288	−3.5	7.9	39.7
298	−4.0		
308	−4.3		

The adsorbent and MO molecules in solution were both sur-rounded by a tightly bounded hydration layer, composed by the highly ordered water molecules. When the MO molecules migrated to approach the adsorbent, the ordered water mole-cules would be compelled and released, resulting in decreas-ing the degree of freedom of MO molecules and increasing the degree of freedom of water molecules. It seemed that the increasing entropy of water molecules overweighed the decreasing entropy of MO molecules, thus causing the posi-tive value of ΔS [43]. The positive value of ΔH revealed that the adsorption process was endothermic, illustrating that an increase of temperature might be beneficial to the adsorption of MO onto CS-Fe@Fe$_3$O$_4$.

3.3.8. Regeneration and reusability

For practical and economic applicability of the prepared adsorbent, it was very important that the absorbent could be reused for the adsorption by desorption and regeneration. The adsorption of MO onto CS-Fe@Fe$_3$O$_4$ is mainly due to complex-ation. Therefore, the dye-loaded absorbent was treated with an alkaline solution for desorption and in an acidic solution for regeneration. The desorption experiment was carried out by using 0.1 M NaOH, Na$_2$CO$_3$ and NaHCO$_3$. And the desorp-tion efficiency was 90.17%, 79.58% and 86.59%, respectively. In addition, many reports suggested that NaOH solution was an effective desorbent [4,44,45]. Hence, we selected NaOH solution as the desorbent in this study. Then, we used NaOH solutions with different concentrations to desorb MO from the CS-Fe@Fe$_3$O$_4$. The results showed that 0.05 M NaOH solution could achieve the highest desorption efficiency at around 94%. After the desorption process, the adsorbent was regenerated by using a 0.1 M HCl solution and drying. Then the regener-ated adsorbent could be reused in the following experiments.

The adsorption and desorption efficiency of MO on CS-Fe@Fe$_3$O$_4$ for five cycles of adsorption–desorption–regeneration are presented in Fig. 11. It showed that the adsorption efficiency remained at about 95%, which indicated that the adsorption sites on the surface of CS-Fe@Fe$_3$O$_4$ were highly reversible.

3.3.9. Adsorption mechanism

Fig. 12 shows the most probable mechanism for the adsorption of MO onto the surface of the CS-Fe@Fe$_3$O$_4$. When the CS-Fe@Fe$_3$O$_4$ was added into the MO containing aqueous solution, the free sulfonic groups in the MO molecules would replace the coordination sites of the water molecules in the Fe coordination sphere, resulting in the removal of MO from solution and the formation of a more stable chelated structure, which could be confirmed by the TG-DTG analysis of the CS-Fe@Fe$_3$O$_4$ before and after adsorption.
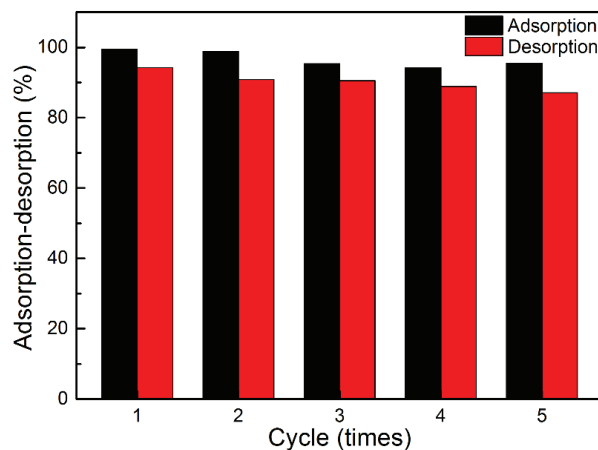

Fig. 11. Adsorption–desorption of MO on CS-Fe@Fe$_3$O$_4$ for five cycles.

In the process of desorption, the hydroxide ions could break the chelation between MO and CS-Fe@Fe$_3$O$_4$ and bind with the Fe centers. Afterwards, the desorbed adsorbent could be regenerated by using hydrogen ions, thus neutral-izing the hydroxide ions and producing water molecules to complete the coordination spheres. Therefore, the CS-Fe@Fe$_3$O$_4$ adsorbent could efficiently adsorb the target dye and achieve the desorption and regeneration, showing its high practical value.

Table 4 shows the CS-Fe@Fe$_3$O$_4$ presented a prominent adsorption capacity for MO as compared with various other reported adsorbents in recent years. It showed that the CS-Fe@Fe$_3$O$_4$ had the highest MO adsorption capacity among those related publications available. Hence, the resultant CS-Fe@Fe$_3$O$_4$ could serve as a promising adsorbent for dye-polluted wastewater remediation.

4. Conclusion

In this study, an economical and practical magnetic adsor-bent, CS-Fe@Fe$_3$O$_4$, was successfully synthesized through chelation between cheap and environmentally friendly chi-tosan and iron ions. Fe$_3$O$_4$ particles were used to introduce magnetic property. The MO could be efficiently removed via the strong chelation between sulfonic groups in a wide range of pH values, while the doped Fe$_3$O$_4$ nanoparticles had almost no negative effect on the adsorption property. In the kinetics analysis, the pseudo-second-order model gave the best fit, suggesting that the chemisorption was a rate-limiting step. The adsorption isotherm data fitted well with the Langmuir model and the maximum adsorption capacities of MO were 1,087.0, 1,149.4 and 1,219.5 mg/g at temperatures of 288, 298 and 308 K, respectively. The negative free energy (ΔG) and the positive enthalpy (ΔH) and entropy (ΔS) indicated the adsorption reactions were spontaneous, endothermic and thermodynamically favorable. Additionally, this adsorbent could be regenerated and reused effectively. In summary, this study suggested that CS-Fe@Fe$_3$O$_4$ could be utilized as a promising adsorbent to effectively remove azo dyes, mean-while its easy separation and convenient recycling property implied its potential application in industrial wastewater treatment.
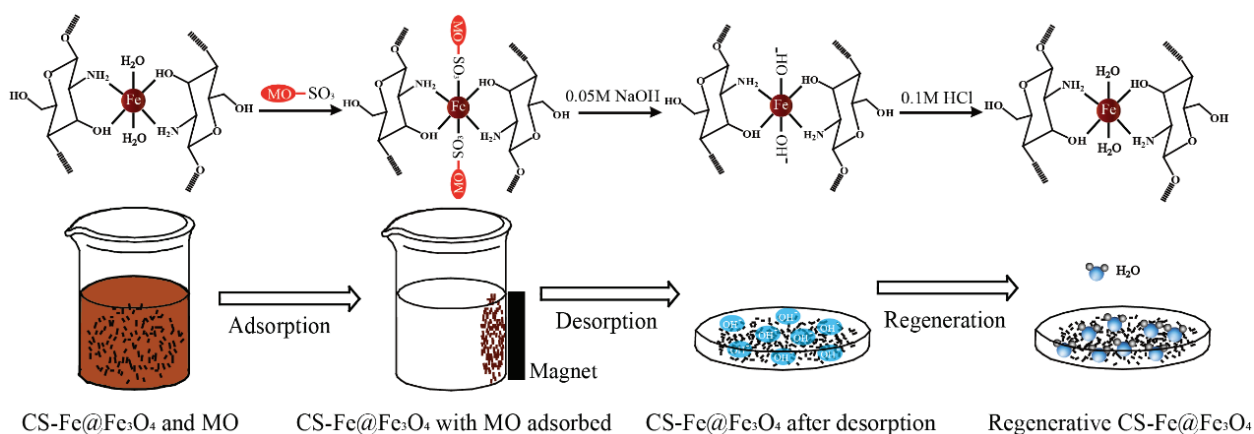
Fig. 12. The schematic diagram of adsorbing MO onto CS-Fe@Fe$_3$O$_4$.

Table 4
Comparison of the adsorption capacity of CS-Fe@Fe$_3$O$_4$ for MO removal with various chitosan-based absorbents

Adsorbents	Adsorption capacity (mg/g)	Reference
Glutaraldehyde cross-linked magnetic chitosan nanocomposites (MCNPs)	758	[26]
Porous chitosan aerogels doped with graphene oxide (CSGO aerogels)	686.89	[16]
Quaternary ammonium salt modified chitosan magnetic composite adsorbent (CS-CTA-MCM)	834.69	[46]
Magnetic chitosan/Al$_2$O$_3$/iron oxide nanoparticles (CANF)	417	[47]
γ-Fe$_2$O$_3$/chitosan composite films	29.41	[48]
Chitosan enwrapping nanosized Fe$_3$O$_4$ (m-CS/Fe$_3$O$_4$/MIL-101)	117	[49]
Chitosan–zinc oxide nanoparticles	481	[50]
Diatomite/chitosan–Fe(III) composite	769.2	[4]
Cross-linked chitosan/bentonite composite (ECCS/BT)	136.8	[20]
CS-Fe@Fe$_3$O$_4$	1,149.4	This study

References

[1] C.K. Mangat, S. Kaur, Efficient removal and separation of anionic dyes from aqueous medium by the application of reverse micelles of cationic surfactants, Desal. Wat. Treat. 52 (2014) 3555–3563.

[2] R. Zandipak, S. Sobhanardakani, Synthesis of NiFe$_2$O$_4$ nanoparticles for removal of anionic dyes from aqueous solution, Desal. Wat. Treat., 57 (2016) 11348–11360.

[3] Z. Deng, X.H. Zhang, K.C. Chan, L. Liu, T. Li, Fe-based metallic glass catalyst with nanoporous surface for azo dye degradation, Chemosphere, 174 (2017) 76–81.

[4] L. Zheng, C. Wang, Y. Shu, X. Yan, L. Li, Utilization of diatomite/chitosan-Fe (III) composite for the removal of anionic azo dyes from wastewater: equilibrium, kinetics and thermodynamics, Colloids Surf. A., 468 (2015) 129–139.

[5] S. Pu, H. Ma, A. Zinchenko, W. Chu, Novel highly porous magnetic hydrogel beads composed of chitosan and sodium citrate: an effective adsorbent for the removal of heavy metals from aqueous solutions, Environ. Sci. Pollut. Res. Int., 24 (2017) 16520–16530.

[6] X. Chen, Z. Wu, D. Liu, Z. Gao, Preparation of ZnO Photocatalyst for the efficient and rapid photocatalytic degradation of azo dyes, Nanoscale Res. Lett., 12 (2017) 143–143.

[7] M. Chenna, R. Chemlal, N. Drouiche, K. Messaoudi, H. Lounici, Effectiveness of a physicochemical coagulation/flocculation process for the pretreatment of polluted water containing Hydron Blue Dye, Desal. Wat. Treat., 57 (2016) 27003–27014.

[8] A. Webster, M.D. Halling, D.M. Grant, Metal complexation of chitosan and its glutaraldehyde cross-linked derivative, Carbohydr. Res., 342 (2007) 1189–1201.

[9] N. Jafari, M.R. Soudi, R. Kasra-Kermanshahi, Biodegradation perspectives of azo dyes by yeasts, Microbiology, 83 (2014) 484–497.

[10] M. Ge, C. Cao, J. Huang, S. Li, S. Zhang, S. Deng, Q. Li, K. Zhang, Y. Lai, Synthesis, modification, and photo/photoelectrocatalytic degradation applications of TiO$_2$ nanotube arrays: a review, Nanotechnol. Rev., 5 (2016) 75–112.

[11] Y. Suerme, R.F. Yilmaz, K. Kayakirilmaz, Removal of textile dye Lanaset Red G from waters by electrochemical degradation and spectrophotometric determination, Desal. Wat. Treat., 53 (2015) 524–529.

[12] S. Pu, R. Zhu, H. Ma, D. Deng, X. Pei, F. Qi, W. Chu, Facile in-situ design strategy to disperse TiO$_2$ nanoparticles on graphene for the enhanced photocatalytic degradation of rhodamine 6G, Appl. Catal. B., 218 (2017) 208–219.
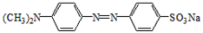
[13] S. Pu, A. Zinchenko, N. Chen, S. Murata, Entrapment and removal of carbon nanotubes and fullerenes by coprecipitation with calcium carbonate beads, ACS Sustain. Chem. Eng., 2 (2014) 2275-2282.

[14] M.S.U. Rehman, I. Kim, J.-I. Han, Adsorption of methylene blue dye from aqueous solution by sugar extracted spent rice biomass, Carbohydr. Polym., 90 (2012) 1314–1322.

[15] V.K. Gupta, R. Kumar, A. Nayak, T.A. Saleh, M.A. Barakat, Adsorptive removal of dyes from aqueous solution onto carbon nanotubes: a review, Adv. Colloid. Interface Sci., 193 (2013) 24–34.

[16] Y. Wang, G. Xia, C. Wu, J. Sun, R. Song, W. Huang, Porous chitosan doped with graphene oxide as highly effective adsorbent for methyl orange and amido black 10B, Carbohydr. Polym., 115 (2015) 686–693.

[17] R. Cheng, S. Ou, B. Xiang, Y. Li, Q. Liao, Equilibrium and molecular mechanism of anionic dyes adsorption onto copper(II) complex of dithiocarbamate-modified starch, Langmuir, 26 (2010) 752–758.

[18] A. Chen, S. Chen, Biosorption of azo dyes from aqueous solution by glutaraldehyde-crosslinked chitosans, J. Hazard. Mater., 172 (2009) 1111–1121.

[19] P. Saha, S. Datta, Assessment on thermodynamics and kinetics parameters on reduction of methylene blue dye using flyash, Desal. Wat. Treat., 12 (2009) 219–228.

[20] L. Zhang, Q. Liu, P. Hu, R. Huang, Adsorptive removal of methyl orange using enhanced cross-linked chitosan/bentonite composite, Desal. Wat. Treat., 57 (2016) 17011–17022.

[21] E. Guibal, T. Vincent, R. Navarro, Metal ion biosorption on chitosan for the synthesis of advanced materials, J. Mater. Sci., 49 (2014) 5505–5518.

[22] A. Pestov, S. Bratskaya, Chitosan and its derivatives as highly efficient polymer ligands, Molecules, 21 (2016) 1–35.

[23] A.B. Sifontes, R.S. Del Toro, E. Avila, E. Canizales, G. Lovera, L. Cubillan, V. Gonzalez, A. Monaco, J.L. Brito, Chitosan templated synthesis of strontium-iron-oxygen nanocrystalline system, Ceram Int., 41 (2015) 13250–13256.

[24] R.N. Shinde, A.K. Pandey, R. Acharya, R. Guin, S.K. Das, N.S. Rajurkar, P.K. Pujari, Chitosan-transition metal ions complexes for selective arsenic(V) preconcentration, Water Res., 47 (2013) 3497–3506.

[25] J. Qu, Q. Hu, K. Shen, K. Zhang, Y. Li, H. Li, Q. Zhang, J. Wang, W. Quan, The preparation and characterization of chitosan rods modified with Fe^{3+} by a chelation mechanism, Carbohydr. Res., 346 (2011) 822–827.

[26] D. Yang, L. Qin, Y. Yang, Efficient adsorption of methyl orange using a modified chitosan magnetic composite adsorbent, J. Chem. Eng. Data, 61 (2016) 3933–3940.

[27] C. Shen, H. Chen, S. Wu, Y. Wen, L. Li, Z. Jiang, M. Li, W. Liu, Highly efficient detoxification of Cr(VI) by chitosan-Fe(III) complex: process and mechanism studies, J. Hazard. Mater., 244 (2013) 689–697.

[28] J. Zhang, N. Chen, Z. Tang, Y. Yu, Q. Hu, C. Feng, A study of the mechanism of fluoride adsorption from aqueous solutions onto Fe-impregnated chitosan, Phys. Chem. Chem. Phys., 17 (2015) 12041–12050.

[29] M. Ge, S. Li, J. Huang, K. Zhang, S.S. Al-Deyab, Y. Lai, TiO_2 nanotube arrays loaded with reduced graphene oxide films: facile hybridization and promising photocatalytic application, J. Mater. Chem. A, 3 (2015) 3491–3499.

[30] D.H.K. Reddy, S.M. Lee, Application of magnetic chitosan composites for the removal of toxic metal and dyes from aqueous solutions, Adv. Colloid Interface Sci., 201 (2013) 68–93.

[31] M.T. Klepka, N. Nedelko, J.-M. Greneche, K. Lawniczak-Jablonska, I.N. Demchenko, A. Slawska-Waniewska, C.A. Rodrigues, A. Debrassi, C. Bordini, Local atomic structure and magnetic ordering of iron in Fe-chitosan complexes, Biomacromolecules, 9 (2008) 1586–1594.

[32] R.B. Hernandez, A.P. Franc, O.R. Yola, A. Lopez-Delgado, J. Felcman, M.A.L. Recio, A.L.R. Merce, Coordination study of chitosan and Fe^{3+}, J. Mol. Struct., 877 (2008) 89–99.

[33] M.H.M. Hussein, M.F. El-Hady, W.M. Sayed, H. Hefni, Preparation of some chitosan heavy metal complexes and study of its properties, Polym. Sci. Ser. A., 54 (2012) 113–124.

[34] S.C. Bhatia, N. Ravi, A magnetic study of an Fe-chitosan complex and its relevance to other biomolecules, Biomacromolecules, 1 (2000) 413–417.

[35] G. Cardenas, P. Orlando, T. Edelio, Synthesis and applications of chitosan mercaptanes as heavy metal retention agent, Int. J. Biol. Macromol., 28 (2001) 167–174.

[36] Z. Osman, A.K. Arof, FTIR studies of chitosan acetate based polymer electrolytes, Electrochim. Acta, 48 (2003) 993–999.

[37] G.R. Mahdavinia, S. Karami, Synthesis of magnetic carboxymethyl chitosan-g-poly(acrylamide)/laponite RD nanocomposites with enhanced dye adsorption capacity, Polym. Bull., 72 (2015) 2241–2262.

[38] M. Munoz, Z.M. de Pedro, N. Menendez, J.A. Casas, J.J. Rodriguez, A ferromagnetic γ-alumina-supported iron catalyst for CWPO. Application to chlorophenols, Appl. Catal. B., 136–137 (2013) 218–224.

[39] G.R. Mandavinia, A. Mosallanezhad, M. Soleymani, M. Sabzi, Magnetic- and pH-responsive kappa-carrageenan/chitosan complexes for controlled release of methotrexate anticancer drug, Int. J. Biol. Macromol., 97 (2017) 209–217.

[40] S. Sen Gupta, K.G. Bhattacharyya, Kinetics of adsorption of metal ions on inorganic materials: a review, Adv. Colloid Interface Sci., 162 (2011) 39–58.

[41] G. Crini, Non-conventional low-cost adsorbents for dye removal: a review, Bioresour. Technol., 97 (2006) 1061–1085.

[42] H. Mittal, A. Maity, S.S. Ray, The adsorption of Pb^{2+} and Cu^{2+} onto gum ghatti-grafted poly(acrylamide-co-acrylonitrile) biodegradable hydrogel: isotherms and kinetic models, J. Phys. Chem. B., 119 (2015) 2026–2039.

[43] G.D. Sheng, D.D. Shao, X.M. Ren, X.Q. Wang, J.X. Li, Y.X. Chen, X.K. Wang, Kinetics and thermodynamics of adsorption of ionizable aromatic compounds from aqueous solutions by as-prepared and oxidized multiwalled carbon nanotubes, J. Hazard. Mater., 178 (2010) 505–516.

[44] W. Zhang, H. Yang, L. Dong, H. Yan, H. Li, Z. Jiang, X. Kan, A. Li, R. Cheng, Efficient removal of both cationic and anionic dyes from aqueous solutions using a novel amphoteric straw-based adsorbent, Carbohydr. Polym., 90 (2012) 887–893.

[45] Y.F. Lin, H.W. Chen, P.S. Chien, C.S. Chiou, C.C. Liu, Application of bifunctional magnetic adsorbent to adsorb metal cations and anionic dyes in aqueous solution, J. Hazard. Mater., 185 (2011) 1124–1130.

[46] R. Li, P. Li, J. Cai, S. Xiao, H. Yang, A. Li, Efficient adsorption of both methyl orange and chromium from their aqueous mixtures using a quaternary ammonium salt modified chitosan magnetic composite adsorbent, Chemosphere, 154 (2016) 310–318.

[47] B. Tanhaei, A. Ayati, M. Lahtinen, M. Sillanpaa, Preparation and characterization of a novel chitosan/Al_2O_3/magnetite nanoparticles composite adsorbent for kinetic, thermodynamic and isotherm studies of Methyl Orange adsorption, Chem. Eng. J., 259 (2015) 1–10.

[48] R. Jiang, Y. Fu, H. Zhu, J. Yao, L. Xiao, Removal of methyl orange from aqueous solutions by magnetic maghemite/chitosan nanocomposite films: adsorption kinetics and equilibrium, J. Appl. Polym. Sci., 125 (2012) E540–E549.

[49] L. Liu, J. Ge, L.-T. Yang, X. Jiang, L.-G. Qiu, Facile preparation of chitosan enwrapping Fe_3O_4 nanoparticles and MIL-101(Cr) magnetic composites for enhanced methyl orange adsorption, J. Porous Mater., 23 (2016) 1363–1372.

[50] M. Khajeh, A.R. Golzary, Synthesis of zinc oxide nanoparticles-chitosan for extraction of methyl orange from water samples: Cuckoo optimization algorithm-artificial neural network, Spectrochim. Acta, Part A., 131 (2014) 189–194.

Supporting information

1. Properties of methyl orange

Methyl orange (MO) is a kind of normal anionic dyes with existence of nitrogen–nitrogen double bonds, which is mainly used as acid and alkali titration indicator and also get wide application in printing and dyeing textiles industries [1]. The basic information of MO is listed in a table as followed.

The basic information of methyl orange

Dye	Molar mass (g/mol)	Structure formula	Molecular formula
Methyl orange	327.3	(CH₃)₂N—⬡—N=N—⬡—SO₃Na	$C_{14}H_{14}N_3O_3SNa$

2. Preparation of CS-Fe

The non-magnetic Fe-crosslinked chitosan (CS-Fe) was prepared under the same condition with CS-Fe@Fe_3O_4.1.0 g CS was dissolved in 50 mL 0.1 M $FeCl_3$ aqueous solution, and the mixture was magnetically stirred for 4 h. Next, precipitation was obtained by adding ethanol into the above mixture. The precipitated solid was washed with ethanol several times to remove the excess iron ions and dried at 80°C under vacuum conditions. Furthermore, the obtained solid was intensively grinded, and slowly placed into a 5% glutaraldehyde ethanol solution for 2 h at 30°C. Thereafter, the composites were collected through an external magnetic field and washed with DI water. After vacuum drying at 80°C, the CS-Fe was obtained.

3. Adsorption kinetics

The linear forms of the pseudo-first-order rate model:

$$\ln(q_e - q_t) = \ln q_e - k_1 t \tag{1}$$

and the linear forms of the pseudo-second-order rate model:

$$\frac{t}{q_t} = \frac{1}{k_2 q_e^2} + \frac{t}{q_e} \tag{2}$$

where q_e (mg/g) and q_t (mg/g) are the adsorption capacity at equilibrium and at time t, k_1 and k_2 (1/min) are the pseudo-first-order and pseudo-second-order adsorption rate constant.

4. Adsorption isotherm

The Langmuir adsorption isotherm assumes that the adsorbate on the surface of the adsorbent is a monolayer adsorption and the binding sites are distributed evenly on the surface of the adsorbent [2], and can be expressed by Eq. (3):

$$\frac{1}{q_e} = \frac{1}{q_{max}} + \frac{1}{q_{max} k_L} \frac{1}{c_e} \tag{3}$$

where q_e (mg/g) is the adsorption capacity at equilibrium, q_{max} (mg/g) is the maximum adsorption capacity of the adsorbent,

c_e (mg/L) is the concentration of the adsorbate at equilibrium and k_L is the Langmuir isotherm constant.

The Freundlich isotherm is an empirical model used to describe heterogeneous adsorption systems [2] and can be expressed by Eq. (4):

$$\ln q_e = \ln k_F + \frac{1}{n} \ln c_e \tag{4}$$

where k_F is the Freundlich isotherm constant and $1/n$ is a dimensionless coefficient related to the adsorption strength.

The Tempkin isotherm model can explain the interactions between adsorbent and adsorbate [2] and can be expressed by Eq. (5):

$$q_e = \beta \ln k_T + \beta \ln c_e \tag{5}$$

where β (K, β = (RT/b)) is the absolute temperature, R (8.314 J/(mol·K)) is the ideal gas constant, b is related to the heat of adsorption and k_T (L/min) is the equilibrium binding constant corresponding to the maximum binding energy.

The Dubinin–Kaganer–Radushkevich isotherm model is mainly used to determine the nature of adsorption and estimate the apparent energy of adsorption (E, kJ/mol) [2], and can be expressed by Eqs. (6)–(8).

$$\ln q_e = \ln Q_m - \beta \varepsilon^2 \tag{6}$$

$$\varepsilon = RT \ln \left(1 + \frac{1}{c_e} \right) \tag{7}$$

$$E = \frac{1}{(2\beta)^{1/2}} \tag{8}$$

where Q_m (mg/g) is the maximum adsorption capacity and β (mol² kJ²) is a constant related to E.

The Flory–Huggins isotherm model represents the degree of surface coverage of the adsorbate molecules onto the surface of adsorbent [2] and can be expressed by Eq. (9).

$$\log \left(\frac{\theta}{c_0} \right) = \log(k_a) + n \log(1 - \theta) \tag{9}$$

where $\theta = (1 - c_e/c_0)$ is the degree of the surface coverage, n is the number of adsorbate molecules adsorbing on the surface of the CS-Fe@Fe_3O_4 and k_a is the equilibrium adsorption coefficient.

5. Adsorption thermodynamics

Thermodynamics equations as followed:

$$\Delta G = -RT \ln K_0 \tag{10}$$

$$\ln K_0 = \frac{\Delta S}{R} - \frac{\Delta H}{RT} \tag{11}$$

where T (K) is the absolute temperature, R (8.314 J/(mol·K)) is the ideal gas constant, K_0 is the distribution coefficient, which can be calculated from a plot of $\ln(q_e/c_e)$ vs. c_e. The enthalpy change (ΔH) and the entropy (ΔS) can be calculated from a plot of $\ln K_0$ vs. $1/T$.
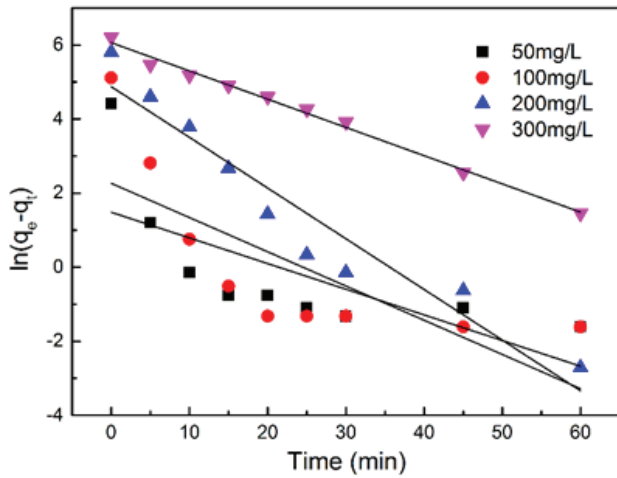
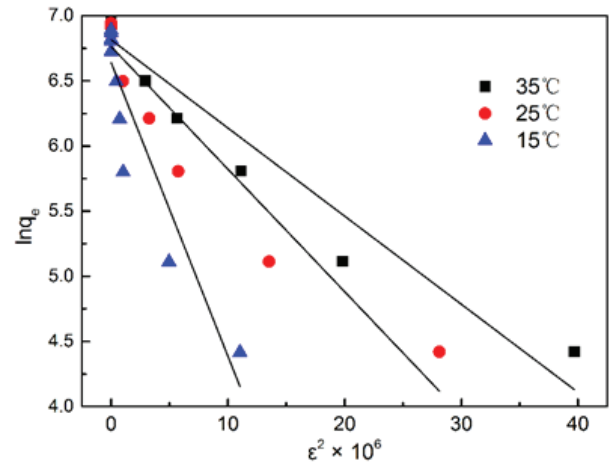Fig. S1. Plot for the pseudo-first-order kinetic model for the adsorption of MO onto CS-Fe@Fe$_3$O$_4$.

Fig. S4. Plot for Dubinin–Kaganer–Radushkevich isotherm model for the adsorption of MO onto CS-Fe@Fe$_3$O$_4$.
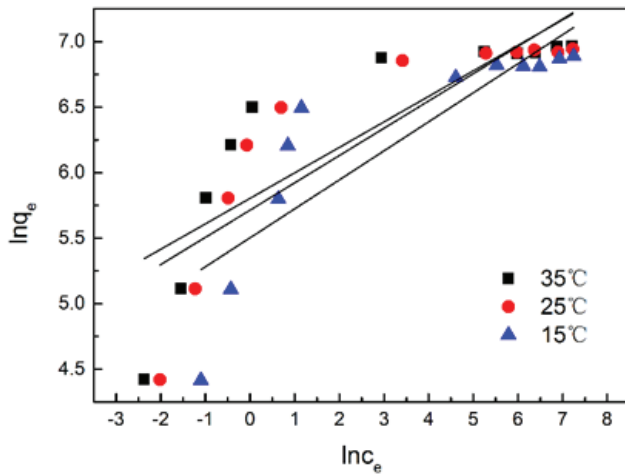

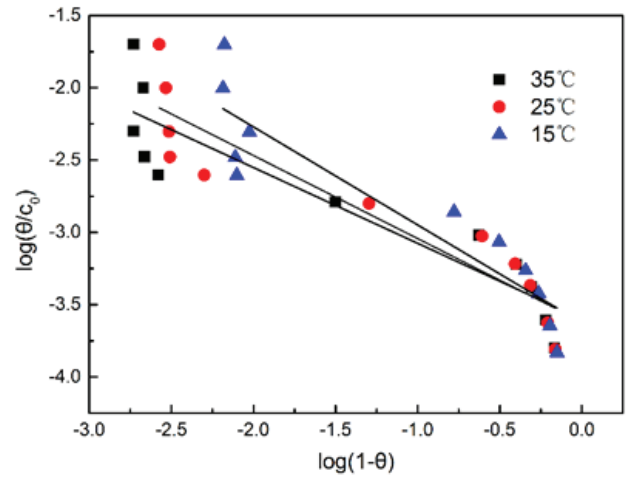Fig. S2. Plot for Freundlich isotherm model for the adsorption of MO onto CS-Fe@Fe$_3$O$_4$.

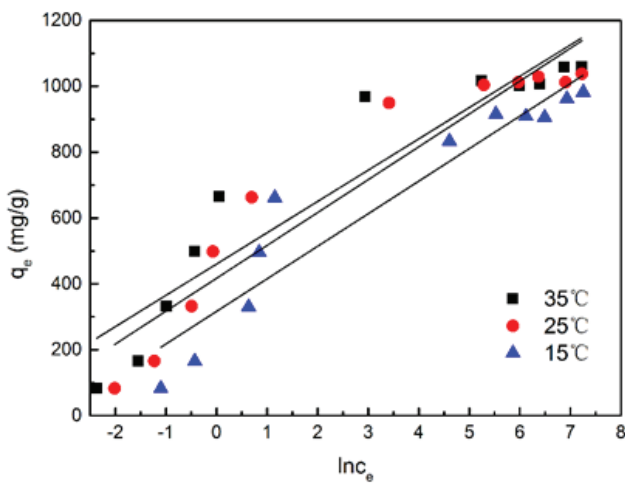Fig. S5. Plot for Flory–Huggins isotherm model for the adsorption of MO onto CS-Fe@Fe$_3$O$_4$.

References

[1] S. Netpradit, P. Thiravetyan, S. Towprayoon, Adsorption of three azo reactive dyes by metal hydroxide sludge: effect of temperature, pH, and electrolytes, J. Colloid Interface Sci., 270 (2004) 255–261.

[2] H. Mittal, A. Maity, S.S. Ray, The adsorption of Pb^{2+} and Cu^{2+} onto gum ghatti-grafted poly(acrylamide-co-acrylonitrile) biodegradable hydrogel: isotherms and kinetic models, Appl. Catal. B., 119 (2015) 2026–2039.

Fig. S3. Plot for Tempkin isotherm model for the adsorption of MO onto CS-Fe@Fe$_3$O$_4$.